MATERIALS CHEMISTRY
FRONTIERS

REVIEW

View Article Online
View Journal | View Issue

Cite this: *Mater. Chem. Front.*, 2025, **9**, 1954

Cation doping engineering of metal halide perovskites for high-energy X-ray exploration

Guiqiang Pu,†[a] Rufeng Wang,†[a] Yangmin Tang,[b] Junnan Song*[a] and Jiacheng Wang*[ab]

Received 14th March 2025,
Accepted 24th April 2025

DOI: 10.1039/d5qm00236b

rsc.li/frontiers-materials

Although metal halide perovskites (MHPs) have shown great advantages as scintillators due to their high quantum efficiency, short luminescence lifetime, low preparation cost, and ease of processing, their further commercialization is still limited due to the challenges such as poor radiative stability, reabsorption, and mismatch between their performance and applications. It is noteworthy that cation doping engineering has been evidenced as an effective solution to overcome these problems faced by MHPs scintillators. To this end, we provide a comprehensive summary of cationic doping engineering used for MHPs scintillators. Foundational theoretical knowledge, including configuration of MHPs and cation doping mechanisms, is first introduced. Multiple technical methods used to introduce impurity cations into MHPs are also discussed. We then discuss in detail the positive impact of cation doping engineering on the scintillation performances of MHPs and their corresponding advanced applications. Finally, we explore the future prospects of cation-doped MHPs scintillators in light of recent advances. This review aims to inspire researchers to explore the next generation of cation-doped MHPs scintillators and to extend their applications.

1. Introduction

Scintillators can convert high-energy rays (such as X- or γ-ray) or particles (such as α-particles, β-particles and neutrons) into low-energy visible photons, and are widely used in medical diagnosis, safety inspection, nuclear monitoring, and high-energy physics.[1,2] Traditional scintillators can be roughly divided into two categories, including inorganic or organic scintillators.[3] Inorganic scintillators are widely used as commercial scintillators because of their high frequency number and density, which show high X-ray absorption capacity. NaI:Tl and CsI:Tl are the earliest single crystal scintillators synthesized in 1949, with high optical yields of 43 000 and 66 000 photons per MeV, respectively.[4,5] However, their commercialization applications are limited by long decay time (>230 ns)

[a] *Zhejiang Key Laboratory for Island Green Energy and New Materials, Institute of Electrochemistry, School of Materials Science and Engineering, Taizhou University, Taizhou, Zhejiang 318000, China. E-mail: jiacheng.wang@tzc.edu.cn*
[b] *State Key Laboratory of High-Performance Ceramics and Superfine Microstructure, Shanghai Institute of Ceramics, Chinese Academy of Sciences, Shanghai 200050, China*
† Guiqiang Pu and Rufeng Wang contributed equally to this work.

Guiqiang Pu

Dr. Guiqiang Pu is currently employed at Taizhou University, Zhejiang, China. He obtained his PhD from the National University of Singapore under the guidance of Professor Zhen Li and Xiaogang Liu in 2024. His research interest is focused on organic/inorganic optoelectronic functional materials and nonlinear luminescent materials.

Rufeng Wang

Rufeng Wang received his BEng from Hangzhou Dianzi University in 2024. He is currently a master degree candidate in Prof. Jiacheng Wang's research group. His research focuses on inorganic scintillation luminescent materials.

and heavy hygroscopicity. BaF_2 is also an inorganic scintillator with the shortest decay time (0.8 ns) but showing a very low light yield of 1430 photons per MeV.[5] In contrast, $Bi_4Ge_3O_{12}$ (BGO) is a mechanically stable inorganic scintillator with proportional properties and is one of the most commonly used scintillators.[6,7]

The term "perovskite" was initially applied to $CaTiO_3$, a mineral discovered in 1839 by German mineralogist Gustav Rose and named after Russian mineralogist Lev Perovski.[8,9] The term currently refers to compounds isostructural with $CaTiO_3$, with the formula ABX_3. In this configuration, B-site cations coordinate with six X-site anions to form $[BX_6]^{4-}$ octahedra, while A-site cations occupy interstitial sites within a three-dimensional framework of corner-sharing $[BX_6]^{4-}$ octahedra. Significantly, recent studies demonstrated that metal halide perovskites (MHPs) have emerged as a novel class of scintillator materials owing to their high quantum efficiency, short luminescence lifetime, low preparation cost, and ease of processing. The incorporation of high atomic number (Z) elements (such as Cs^+, Pb^{2+}, Bi^{3+} cations and I^- anions) provides enhanced X-ray attenuation coefficients and remarkable light yield, reaching up to 90 000 photons per MeV at 77 K.[10] Additionally, simple synthesis processes enable relatively easy preparation of polycrystalline thin films, single crystals and nanocrystals (NCs).[11,12] Despite significant advances in MHPs scintillators, their practical implementation remains constrained by intrinsic limitations, including instability under light/environmental exposure,[13] toxicity concerns from lead content,[12] and trade-offs between the light yield and decay lifetime.[10]

Cation doping is an effective method for introducing specific impurity ions into a substrate to improve the photoelectric properties of the substrate materials.[14,15] In MHPs scintillators, cation doping is also a popular technique to stabilize the crystal structure,[16] regulate luminescence properties,[17,18] and improve the performance of optoelectronic devices.[19–21] Meanwhile, due to its special ionic crystal structure,[13,22] the cation doping of MHPs (in the form of ABX_3) is easier and more diverse than that of conventional NCs. Although great progress has been made in cation doping of MHPs scintillators,[23,24] there is a lack of a comprehensive review that systematically summarizes this technology in terms of theoretical foundation, preparation strategies, conformational relationships, and advanced applications.

Accordingly, we systematically discuss recent advances in cationic doping engineering of MHPs scintillators in this review (Fig. 1). Firstly, the key theoretical knowledge is presented, including the basic structure of MHPs, doping mechanisms and the classification of doped cations. Construction strategies including the thermal injection method and ion exchange method are equally discussed to realize cationic doping engineering. The influence of cationic doping engineering on the scintillation properties of MHPs is then emphasized, such as the light yield, stability and decay time. The improvement of these key parameters opens up a wider range of applications for MHPs scintillators in medical imaging X-ray or high-energy particle detection. Finally, we present future challenges and prospects for cation doping engineering of MHPs scintillators.

2. Theoretical knowledge of cation-doped MHPs scintillators

In the past few years, cation doping engineering has become a necessary means to improve the performance of MHPs

Yangmin Tang

Yangmin Tang received her BS degree from Central South University (CSU). She is now a PhD candidate at the State Key Laboratory of High-Performance Ceramics and Superfine Microstructure, Shanghai Institute of Ceramics, Chinese Academy of Sciences (SICCAS) under the supervision of Prof. Jiacheng Wang. Her current research focuses on scintillation materials.

Junnan Song

Dr. Junnan Song is currently employed at Taizhou University, Zhejiang, China. She obtained her PhD from the Nanjing University of Aeronautics and Astronautics, Jiangsu, China. Her research interests are focused on the design, synthesis and characterization of small molecule electrocatalytic materials.

Jiacheng Wang

Dr. Jiacheng Wang (FRSC) is currently a full professor at Taizhou University, Zhejiang, China, and head of Zhejiang Key Laboratory for Island Green Energy and New Materials. He obtained his PhD from the Shanghai Institute of Ceramics, Chinese Academy of Sciences (SICCAS) in 2007. From 2013 to 2023, he was a professor at SICCAS. His present research focuses on rational design and preparation of advanced functional materials for energy transformation and photoluminescence.

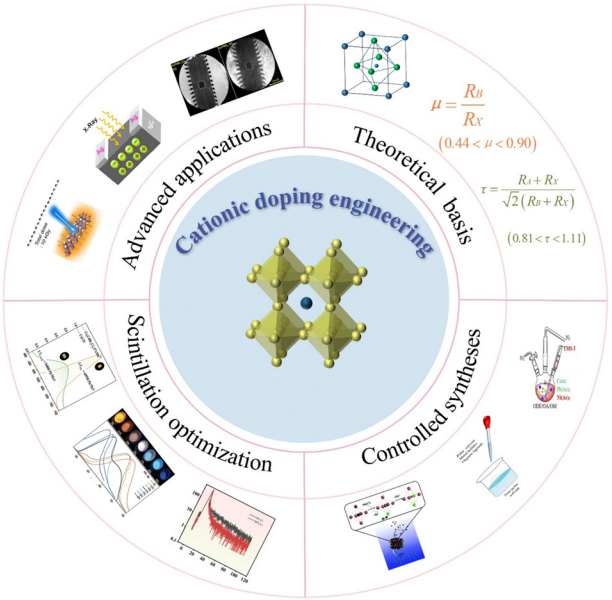

Fig. 1 Description of cationic doping engineering from the aspects of theoretical basis, syntheses, scintillation optimization and advanced applications of MHP scintillators.

scintillators. Undoubtedly, mastering the structure of MHPs and the basic theory of cationic doping is the prerequisite for cationic doping engineering. In this part, the basic structure of MHPs and the classification of cation-doped MHPs scintillators are discussed in detail.

2.1. Configurations of MHPs

In general, MHPs with the ABX_3 framework usually present a six-coordinated B site with X by forming an octahedral structure.[25] According to the arrangement of octahedrons and A-sites, MHPs can be divided into four types: zero-dimensional (0D), one-dimensional (1D), two-dimensional (2D) and three-dimensional (3D).[26] Fig. 2 shows the structure of 3D MHPs and other different dimensions at the morphological and molecular levels.[27] In the prototypical ABX_3 structure, the ionic radii of A-, B-, and X-site ions must satisfy the Goldschmidt tolerance factor τ.[28]

$$\tau = \frac{R_A + R_B}{\sqrt{2}(R_B + R_X)} \quad (1)$$

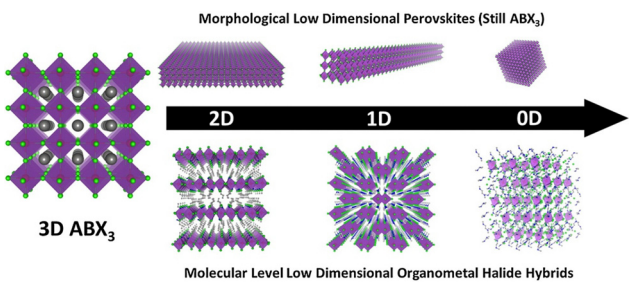

Fig. 2 Typical structures of 0D, 1D, 2D, and 3D MHPs.[27] (Adapted with permission from ref. 27. (Copyright 2019, Elsevier)).

where R_A, R_B, and R_X represent the ionic radii of A-, B-, and X-site elements, respectively. Stable MHPs structures require the tolerance factor τ to range from 0.813 to 1.107, with the optimal cubic phase formation occurring at $0.9 \leq \tau \leq 1$.[29–31] Cations with inappropriate ionic radii (either too large or small) cause structural distortion, leading to cubic lattice warping and eventual decomposition.[32] The tolerance factors for various A-site cations in ABX_3 can be obtained *via* eqn (1). In addition to the tolerance factor τ, octahedral factor μ is used as an additional semi-empirical geometric parameter to evaluate the stability of the octahedron.[33] μ is defined as

$$\mu = \frac{R_B}{R_X} \quad (2)$$

The μ values in the range of 0.442–0.895 favour the formation of stable $[BX_6]^{4-}$ octahedra. Based on the above analysis, it is certain that the choice of A-site and B-site cations should not only meet the range of tolerance factor τ, but also meet the requirements of octahedral factor μ.[33]

2.2. Cation doping mechanisms in MHPs scintillators

In general, cation doping engineering is realized by occupying the A- or B-site of the MHPs. The cations used for doping at the A-site are usually some monovalent metal ions or organic functional groups, whereas metal cations with higher valence can be populated to the B site. Due to the doping of cations, not only their stability and scintillation performance are improved, but also their band structure and photophysical properties have undergone great changes.[34–37] In the past few years, various metal ions including Sn^{2+}, Bi^{3+}, Mn^{2+}, and rare earth ions (*e.g.* Ce^{3+}, Tb^{3+}, Eu^{3+}) have been doped into MHPs scintillators, and this prominent material has been endowed with a wide range of exotic properties.[23,38] Next, we discuss two situations in detail.

2.2.1. A-site doping

2.2.1.1. Organic cations. A-site doped ions encompass organic cations including methylamine (MA^+) and formamidine (FA^+).[39] For instance, Huang *et al.* synthesized indium–halide perovskites containing various organic amine cations, including MA_4InCl_7, EA_4InCl_7, PA_6InCl_9, and TTA_2InCl_5 (where MA^+ = methylamine, EA^+ = ethylamine, PA^+ = aniline, and TTA^+ = tetraethylammonium).[40] They further regulated the A-site of the perovskite scintillator by doping antimony ions and introducing another organic amine 2,6-dimethylpiperazine. Yuan *et al.* obtained $MAPbI_3$ based high-quality three-dimensional $DMAMAPbI_3$ and $GAMAPbI_3$ by adding DMA (dimethylammonium) and GA (guanidinium) with larger volumes and hydrogen bonds at site A.[41] The newly obtained crystals have smaller defect state density and carrier concentration, and their carrier mobility and lifetime are effectively increased.

2.2.1.2. Inorganic cations. A-site doped ions also include inorganic cations such as cesium (Cs^+) and rubidium (Rb^+).[34] Ye *et al.* demonstrated that introducing Rb^+ into the A-site of the MHPs lattice effectively reduced the Cl^- content, suppressed the formation of non-radiative defects, and significantly

enhanced the photoluminescence quantum yield (PLQY).[42] This approach not only enhanced the luminous performance but also maintained the emission wavelength stability required for display applications, thereby providing a novel solution to the performance degradation induced by chlorine. Clara Otero-Martínez *et al.* reported rapid cross-exchange of A-site cations between $APbX_3$ perovskites made of different A cations (Cs^+, FA^+ and MA^+) at room temperature. Surprisingly, both dual (MACs, MAFA, and CsFA) and triple (MACsFA) cationic perovskites could be prepared, whose optical band gap could be fine-tuned by their A-site composition, and the distribution of different cations in the mixed perovskite lattice is uniform.[43]

2.2.2. B-site doping

2.2.2.1. Isovalent doping. The formation energy of the B-site is relatively greater than that of the A-site, which makes the partial substitution of B-site cations in the ABX_3 perovskite more difficult than other sites.[36] The primary motivation for B-site doping in MHPs scintillators includes two aspects: reducing toxic lead content and stabilizing the perovskite phase. The ionic exchange of Pb^{2+} with other divalent cations from the same periodic group (*e.g.*, Ge^{2+} and Sn^{2+}) represents the most straightforward strategy, which has been successfully implemented by multiple research groups.[44–46] Sn emerges as the most viable Pb substitute owing to their shared group position in the periodic table. Therefore, a higher PLQY was obtained during hot injection synthesis by introducing $SnBr_2$ to partially replace $PbBr_2$ and by using more oleic acid and oleylamine.[47] The bivalent metal ion Mn^{2+} has been widely used in doped MHPs scintillators. Zou *et al.* reported that doping Mn^{2+} ions into $Cs_2CdBr_2Cl_2$ achieves a significant increase in PLQY from 11% to 98.52%.[48] Benefiting from near-unity PLQY and minimal self-absorption, the $Cs_2CdBr_2Cl_2$:5%Mn^{2+} perovskite displays outstanding X-ray scintillation performance.

2.2.2.2. Heterovalent doping. Heterovalent doping could also enhance the optical and scintillation properties of MHPs.[49] Zhu *et al.* prepared a series of non-toxic double perovskite $Cs_2Ag_{0.6}Na_{0.4}In_{1-y}Bi_yCl_6$ single crystals with variable Bi^{3+} ion content. The introduction of an appropriate amount of Bi^{3+} ions not only improved the radiative luminescence output but also accelerated the radiative recombination.[50] In addition, Pan *et al.* have successfully developed various lanthanide doped $CsPbCl_3$ perovskites. The introduction of lanthanide ions could significantly improve the PLQY of $CsPbCl_3$ perovskites, and it was easy to achieve full visible light emission or even near-infrared emission.[51] Angshuman Nag *et al.* reported that Bi^{3+}/Ln^{3+} (Ln^{3+} = Er^{3+}, Yb^{3+}) ion co-doped $Cs_2AgInCl_6$ double perovskite materials emit near-infrared light at 1540 or 994 nm under near-ultraviolet excitation. Compared with the undoped samples, the near-infrared luminescence intensity of the co-doped samples was increased by about 45 times and 27 times, respectively.[52]

3. Construction strategy of cation-doped MHPs scintillators

During the synthesis of MHPs scintillators, the cationic dopants are usually implanted into the lattice by ion exchange during or after the main lattice growth stage. However, lattice strain and defects are often generated due to the difference in atomic radius and charge number, which may lead to a surface segregation phenomenon. It is necessary to formulate corresponding construction strategies during doping. Therefore, we summarized several commonly used methods to realize cation doping engineering in MHPs scintillators.

3.1. Hot injection

The hot injection method is a widely used technique for synthesizing MHPs materials. This method features a straightforward preparation process and controllable crystal morphology. It allows flexible selection of doped ion sources including halogenates, acetates, and oleates as cation precursors (Fig. 3a).[53] However, maintaining stable reaction conditions typically requires high-boiling-point solvents (*e.g.*, octadecene) combined with N_2 gas protection.[54–57] Furthermore, MHPs exhibit limited solubility under these high-temperature conditions. Consequently, many studies have used acetate, which is more soluble in high boiling point solvents, in place of traditional halides.[53,58,59] Zhao *et al.* developed a low-temperature solvent direct injection strategy to induce rapid nucleation. Simultaneously, the abrupt solute concentration drop suppresses the overgrowth of NCs while enhancing quality and uniformity, demonstrating potential for scalable manufacturing.[60] Compared with other synthesis methods, the hot injection approach generates localized high-temperature conditions and maintains an inert atmosphere, thereby facilitating many difficult doping reactions. However, the hot injection method is usually suitable for small-scale synthesis in the laboratory, which limits its industrial application.

3.2. Liquid-assisted rapid preparation (LARP)

The LARP technique was initially developed by Zhong and co-workers in 2015 as a synthetic methodology for organic–inorganic hybrid perovskite materials (Fig. 3b).[63] The fundamental procedure comprises two principal stages. Initially, a precursor solution is formulated by dissolving $MA^+/Cs^+/FA^+$ cations, Pb^{2+} ions, and halide precursors, along with capping ligands such as alkyl amines and carboxylic acids, in polar solvents like dimethylformamide (DMF) or dimethyl sulfoxide (DMSO). Thereafter, under vigorous agitation, the precursor solution is introduced into an anti-solvent such as acetone, toluene, or hexane. Compared with the hot injection method, the reaction conditions of LARP are relatively mild and controllable. However, due to the high sensitivity of the resulting MHPs to polar solvents, they often suffer from damage or partial dissolution during the purification process. B-site cation-doped MHPs can be synthesized by introducing a precursor solution containing dopants into the anti-solvent. Conversely, undoped MHPs can be obtained by omitting the dopant. By carefully selecting the types of precursors and capping ligands, low-dimensional cation doped MHPs can be successfully synthesized.[64–66]

3.3. Ion exchange

Unlike the above approaches, ion exchange is typically performed after synthesizing MHPs NCs and thin films. For instance,

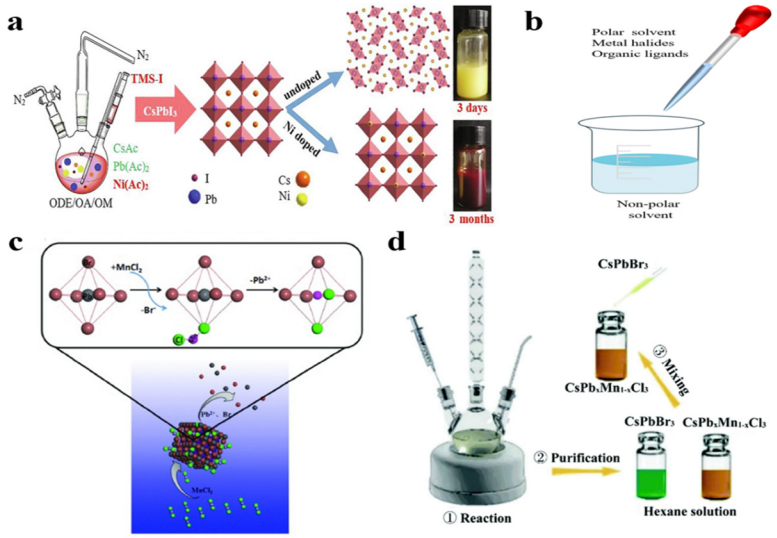

Fig. 3 (a) Hot injection method for preparing MHPs.[53] (b) Liquid-assisted rapid preparation. (c) Schematic diagram of anion-driven cation exchange.[61] (d) Reversible ion exchange between $CsPbCl_3$ and $CsMnCl_3$.[62] (Adapted with permission from ref. 53. (Copyright 2021, Elsevier),[61] (Copyright 2017, Wiley-VCH Verlag GmbH & Co. KGaA, Weinheim) and ref. 62 (Copyright 2017, Royal Society of Chemistry)).

colloidal MHPs are conventionally synthesized and dispersed in toluene/hexane solvent systems. Subsequently, a predetermined ratio of solid dopant or dopant precursor solution is introduced into the above dispersion under vigorous stirring. For cationic doping of MHPs films, the general step involves preparing MHPs films and then immersing them in a solution containing dopant cation ions.[67]

Huang and his colleagues proposed a simple but effective strategy termed halide exchange-driven cation exchange for rapid B-site cation exchange in 2017 (Fig. 3c).[61] However, this process still required a long time (2 days) for completion due to the limited solubility of dopant precursors in non-polar solvents at room temperature.[61] Enhancing the dopant precursor solubility and the chance of the dopant colliding with the subject could significantly improve the doping efficiency. This was demonstrated by mixing a colloidal solution of Mn^{2+} doped $CsPbCl_3$ with $CsPbBr_3$ (Fig. 3d), which successfully reduced the reaction time to 1 hour.[62] Ion exchange is often used to maintain the shape of a material while changing its composition, resulting in a product that is not available through direct synthesis. Nevertheless, compared with the other two methods, this approach requires significantly longer preparation time.[61,62] Furthermore, alternative strategies including ultrasonic treatment,[68] melt quenching,[69] spin coating,[70,71] and solvothermal methods[72] have been effectively employed for synthesizing cation doped MHPs NCs, thin films, and single crystals.

4. Contribution of cation doping to the scintillation performances of MHPs

In recent years, MHPs scintillators have shown great potential in X-ray imaging and other fields, but most of them still face bottleneck problems such as limited light yield, insufficient stability and hysteresis of attenuation time. It is noteworthy that the scintillation performance of MHPs can be greatly improved by cationic doping engineering. In this part, we summarize the influence of cation doping engineering on the scintillation performance of MHPs in terms of light yield, stability, spectrum, decay time and toxicity mitigation.

4.1. Light yield

As a crucial parameter for characterizing scintillators, light yield reflects the ability of the scintillators to convert high-energy radiation into visible light. This indicator is particularly critical for achieving high-resolution X-ray imaging.[73] A possible strategy to increase the optical yield of MHPs scintillators is to dope cations in the B-site. For instance, Zou *et al.* reported the synthesis of a new 2D $Cs_2CdBr_2Cl_2$ perovskite by a hydrothermal reaction,[48] and they explored the deep ultraviolet absorption characteristics of $Cs_2CdBr_2Cl_2$. The introduction of Mn^{2+} ions produced emission with a large Stokes shift, which could effectively avoid self-absorption, and was conducive to obtaining a high light yield under X-ray excitation. The light yield of $Cs_2CdBr_2Cl_2$:5%Mn^{2+} exceeds 64 950 photons per MeV when using the commercial CsI:Tl scintillator as a reference (Fig. 4a). This light output was significantly better than that of previously reported MHPs scintillators such as $CsPbBr_3$ NCs (21 000 photons per MeV),[74,75] and even higher than that of some conventional bright scintillators (CsI:Tl, 54 000 photons per MeV; GOS, 60 000 photons per MeV).[76,77] Omar F. Mohammed *et al.* obtained a high-performance flexible X- ray scintillator by doping Cs_2AgI_3 with Cu^{2+}, achieving extremely high X-ray detection sensitivity. Both time-resolved measurements and DFT calculations showed that Cu^{2+} doping increased the density of self-trapping excitons, which significantly enhanced the recombination of radiation excitons. They successfully produced a flexible large-area scintillation screen based on Cu-doped Cs_2AgI_3 powder with excellent X-ray scintillation performance, including an

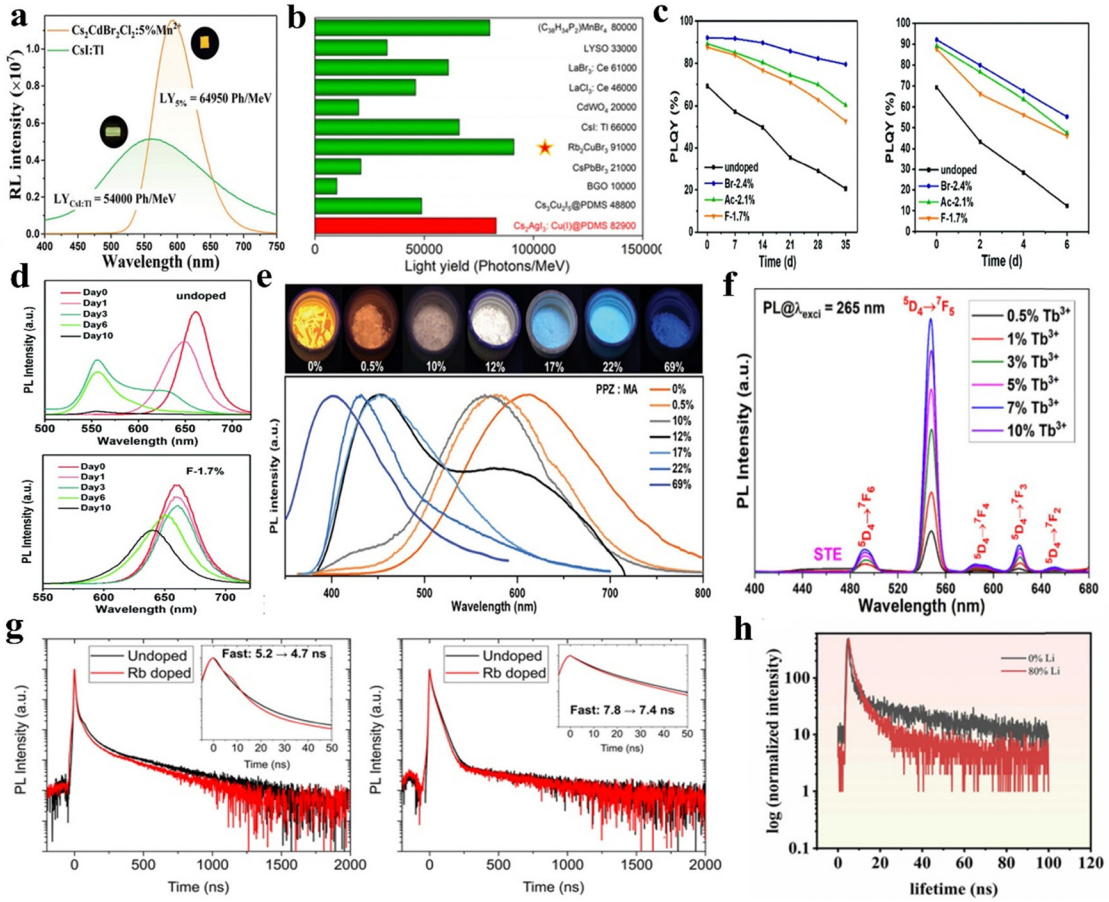

Fig. 4 (a) Radioluminescence spectra of $Cs_2CdBr_2Cl_2$:5%Mn^{2+} and CsI:Tl.[48] (b) Comparison of the light yield of $CsAgI_3$:Cu scintillators with previously reported and commercial scintillators.[78] (c) Left: PLQYs of $CsPbBrI_2$ exposed to the controlled environment (25 ± 1 °C, 20% relative humidity) over time; Right: variation of PLQYs of $CsPbBrI_2$ under continuous 365 nm UV irradiation *versus* exposure duration. (d) Top: Photoluminescence evolution of undoped $CsPbBrI_2$ NCs; Bottom: Photoluminescence evolution of Fe^{2+}-doped $CsPbBrI_2$ NCs under UV illumination.[79] (e) Fluorescence photograph (top) and emission spectrum (bottom) of 2,6-dimethylpiperazine-doped MA_4InCl_7:Sb^{3+} under ultraviolet irradiation.[80] (f) Photoluminescence spectra doped with *x*% Tb^{3+} (*x* = 0.5–10%) $Cs_2NaGdCl_6$.[81] (g) photoluminescence decay profiles of undoped and Rb-doped BA_2PbBr_4. Inset: magnified view of photoluminescence decay curves in the 0–50 ns time window.[82] (h) Photoluminescence decay lifetimes for 0% Li-doped and 80% Li-doped samples.[83] (Adapted with permission from ref. 48. (Copyright 2023, Wiley-VCH GmbH),[78] (Copyright 2022, American Chemical Society),[79] (Copyright 2022, Royal Society of Chemistry),[80] (Copyright 2023, Wiley-VCH GmbH),[81] (Copyright 2024, American Chemical Society),[82] (Copyright 2023, American Chemical Society) and ref. 83 (Copyright 2025, Elsevier B.V.)).

ultra-high yield of 82 900 photons per MeV (Fig. 4b) and an ultra-low detection limit of 77.8 nGy s^{-1}, which is about 70 times lower than the dose for standard medical diagnoses.[78]

4.2. Stability

The crystal structure of MHPs is highly sensitive to polar solvents, especially water. As a result, most MHPs scintillators exhibit poor stability under ambient conditions. In the $CsPbX_3$ system, the stability issue of red-emitting MHPs is particularly prominent, with the most unstable α-$CsPbI_3$ being prone to phase transitions.[84–86] The relatively small cationic radius of Cs^+(1.88 Å) leads to suboptimal tolerance factors in all-inorganic $CsPbX_3$ systems. Partial substitution of Pb^{2+} with smaller B-site cations can shorten B–X bond lengths and stabilize the perovskite structure through reduced octahedral rotation/distortion, thereby enhancing both tolerance factor (improved phase stability) and formation energy (enhanced thermal stability).[87] Chen *et al.* utilized Fe^{2+} ions as dopant ions to enhance the stability of α-$CsPbBrI_2$ NCs, which also reduced the toxic lead content through partial substitution. To investigate the influence of different iron sources, three iron salts ($FeCl_2$, $Fe(Ac)_2$, and FeF_2) were selected for comparison. The results demonstrated that the PLQY of $CsPbBrI_2$ NCs increased from 69.2% to 90% owing to the partial substitution of Pb^{2+} with smaller Fe^{2+} ions. Remarkably, Fe^{2+} doping induced lattice shrinkage, shortened Pb–X bond lengths, inhibited the distortion of $[PbX_6]^{4-}$ octahedra, and enhanced the stability of $CsPbBrI_2$ NCs. After 5 weeks of ambient exposure, the PLQY retained over 60% of its initial value (Fig. 4c and d).[79]

4.3. Spectrum

According to traditional theories and researches, the main function of the cation occupying the A site is to maintain the stability of the crystal structure and balance the charge, and its

atomic orbital does not participate in the composition of the conduction band and the valence band,[88] so researchers generally believe that the A site has no important influence on the luminescence of MHPs scintillators. However, the organic amine cations at the A site can interact with the metal halide coordination polyhedron through hydrogen bonding,[89] thus affecting the degree of distortion of the polyhedron (luminescence center), which may have a significant effect on the luminescence properties. Based on this hypothesis, Huang *et al.* developed a series of MHPs with different organic amine cations, namely MA_4InCl_7, EA_4InCl_7, PA_6InCl_9, and TTA_2InCl_5 (MA^+, EA^+, PA^+, and TTA^+ are methylamine, ethylamine, aniline, and tetraethylammonium cations, respectively).[80] Through an antimony ion doping strategy, the MHPs achieved broad-spectrum warm white light emission covering the visible range (450–850 nm). Interestingly, by introducing the organic amine 2,6-dimethylpiperazine into these antimony-doped MHPs and further regulating the A-site composition, researchers successfully attained broad-spectrum white light emission (Fig. 4e). The luminescence mechanism analysis showed that the white light emission came from the blue light emission of indium chloride doped with 2,6-dimethylpiperazine in MHPs derivatives and the yellow light emission of self-limiting excitons of antimony chloride polyhedron doped with antimony ions, which generated the complementary light emitted by white light. This strategy is also the first case to achieve white light emission through mixed organic amine cation regulation at the A-site of MHPs.

In addition, the spectra can also be regulated by B-site doping. For instance, both undoped and Tb^{3+}-doped $Cs_2NaGdCl_6$ samples with various Tb^{3+} concentrations were successfully synthesized *via* a hydrothermal method. The incorporation of Tb^{3+} ions into $Cs_2NaGdCl_6$ induced an efficient energy transfer process from self-trapping excitons to Tb^{3+} ions (Fig. 4f). This mechanism effectively tuned the emission from blue to green by suppressing the STE emission while enhancing the characteristic green emission at 549 nm (corresponding to the $^5D_4 \rightarrow {}^7F_5$ transition of Tb^{3+}).[81]

4.4. Decay time

Fast attenuating scintillators have sub-nanosecond/nanosecond lifetime and high temporal resolution, and are widely used in nuclear physics, medical diagnostics, and other fields.[1,2] As the demand for radiation detection continues to grow, the requirements for scintillators also increase, and the ultra-fast decay time can achieve good temporal resolution and response rate of the detector.[90] Notably, the decay lifetime of the MHPs scintillators can also be significantly shortened by the doping of suitable cations. Muhammad Danang Birowosuto *et al.* reported Rb-doped BA_2PbBr_4 and PEA_2PbBr_4.[82] The decay times for undoped and Rb-doped BA_2PbBr_4 were measured to be 5.2 and 4.7 ns, respectively. Correspondingly, the decay times for undoped and Rb-doped PEA_2PbBr_4 were 7.8 and 7.4 ns, respectively (Fig. 4g). Obviously, the fast decay times of BA_2PbBr_4 and PEA_2PbBr_4 were greatly reduced after doping with Rb^+ ions. The average attenuation time of BA_2PbBr_4 and PEA_2PbBr_4 doped with Rb^+ is reduced by 15% and 8% respectively.

Silver-based MHPs scintillators have garnered significant attention owing to their short decay lifetimes, positioning them as promising candidates for future applications.[91] The photoluminescence and radioluminescence intensities of Rb_2AgCl_3 were significantly enhanced through a defect modulation strategy combined with an antisolvent method, enabling optimal Li^+ ion doping in the Rb_2AgCl_3 host matrix. Li^+ ion doping reduces defects, thereby suppressing non-radiative relaxation processes and enhancing radiative recombination. At the optimal doping concentration, the scintillator demonstrates remarkable performance with 88.7% quantum efficiency and an ultrafast decay lifetime of 4.6 ns (Fig. 4h), representing a significant improvement over decay lifetime of 11.1 ns for the undoped sample and surpassing most reported scintillators.[83]

4.5. Toxicity mitigation

The photoelectric properties of MHPs have attracted significant attention in the research community over the past few years, but the new technology faces two major challenges, improving long-term stability and reducing Pb content without compromising their performance and stability. At the same time, Pb element is also widely considered to be highly toxic to humans and highly polluting to the environment, so the toxicity of the Pb element in these MHPs devices has hindered its large-scale application. Cation doping of Pb-based perovskites involves the partial substitution of Pb^{2+} with other metal ions to regulate the material properties and mitigate lead toxicity. For instance, Ana Beatriz Ferreira Vitoreti *et al.* doped Sn^{2+} to partially replace Pb^{2+}, reducing the toxicity of Pb while also shortening the bond length between metal cations and halides, thereby improving the stability and enhancing the optical properties.[47]

5. Advanced applications

Since the concept of cation doping engineering was introduced, the advanced applications of MHPs scintillators have entered a new stage. Doping engineering greatly improves a series of advantages such as high spatial resolution and detection sensitivity, which are essential for advanced applications such as X-ray imaging and radiation detection. Next, we discussed advanced applications of MHPs scintillators enabled by cation doping engineering.

5.1. X-ray imaging

X-ray imaging is the most critical application domain for MHPs scintillators. The spatial resolution of X-ray images is crucial for evaluating image quality, as it primarily depends on the inherent properties of the scintillator and the morphology of the scintillator film.[3] X-ray imaging requires higher light output to improve spatial resolution and reduce radiation dose, thereby minimizing patient harm. In addition, the direct band gap characteristics of MHPs typically lead to small Stokes shifts, causing significant self-absorption phenomena. Furthermore,

concentrated band gap transitions induced by exciton-limiting effects can exacerbate self-absorption, thereby reducing photon emission.[92] This phenomenon becomes particularly significant in X-ray imaging applications requiring sub-millimeter-thick scintillator films. Therefore, minimizing scintillator self-absorption represents a critical strategy for enhancing the light yield. Cation incorporation in MHPs structures can effectively amplify the Stokes shift through characteristic emission, thereby improving X-ray imaging performance.

In 2021, Yang *et al.* reported the *in situ* growth of Eu^{3+}-doped $CsPbBr_3$ within a transparent amorphous glass matrix ($CsPbBr_3$:Eu-GC).[93] The $CsPbBr_3$:Eu-GC composite demonstrated superior X-ray imaging performance with a spatial resolution of 15 $lpmm^{-1}$ at 20% MTF, significantly exceeding the 4.1 $lpmm^{-1}$ value observed for pure $CsPbBr_3$-GC under identical conditions (Fig. 5a–d). Xia *et al.* utilized Eu(II) as the B-site ions to develop a novel class of Eu(II)-doped MHPs scintillators.[94] The corresponding scintillator films exhibited an ultra-high X-ray imaging resolution of 27.3 $lpmm^{-1}$. They successfully demonstrated X-ray imaging of joint structures in longiceps specimens containing an implanted metal needle (diameter: 100 μm) under a dose rate of 0.78 μGy s^{-1}, which was 60 times lower than the diagnostic X-ray dose level of 5.5 μGy s^{-1} (Fig. 5e). The imaging system clearly resolved the internal circuitry of a chip driver, as illustrated in Fig. 5f. Furthermore, three concealed objects (coffee bottles, iron knives, and aluminum pots) enclosed in plastic containers (Fig. 5g) were imaged to assess the potential of the AAO@MeEu material for security screening applications. MATLAB simulations further enabled material differentiation through color intensity analysis (Fig. 5h).

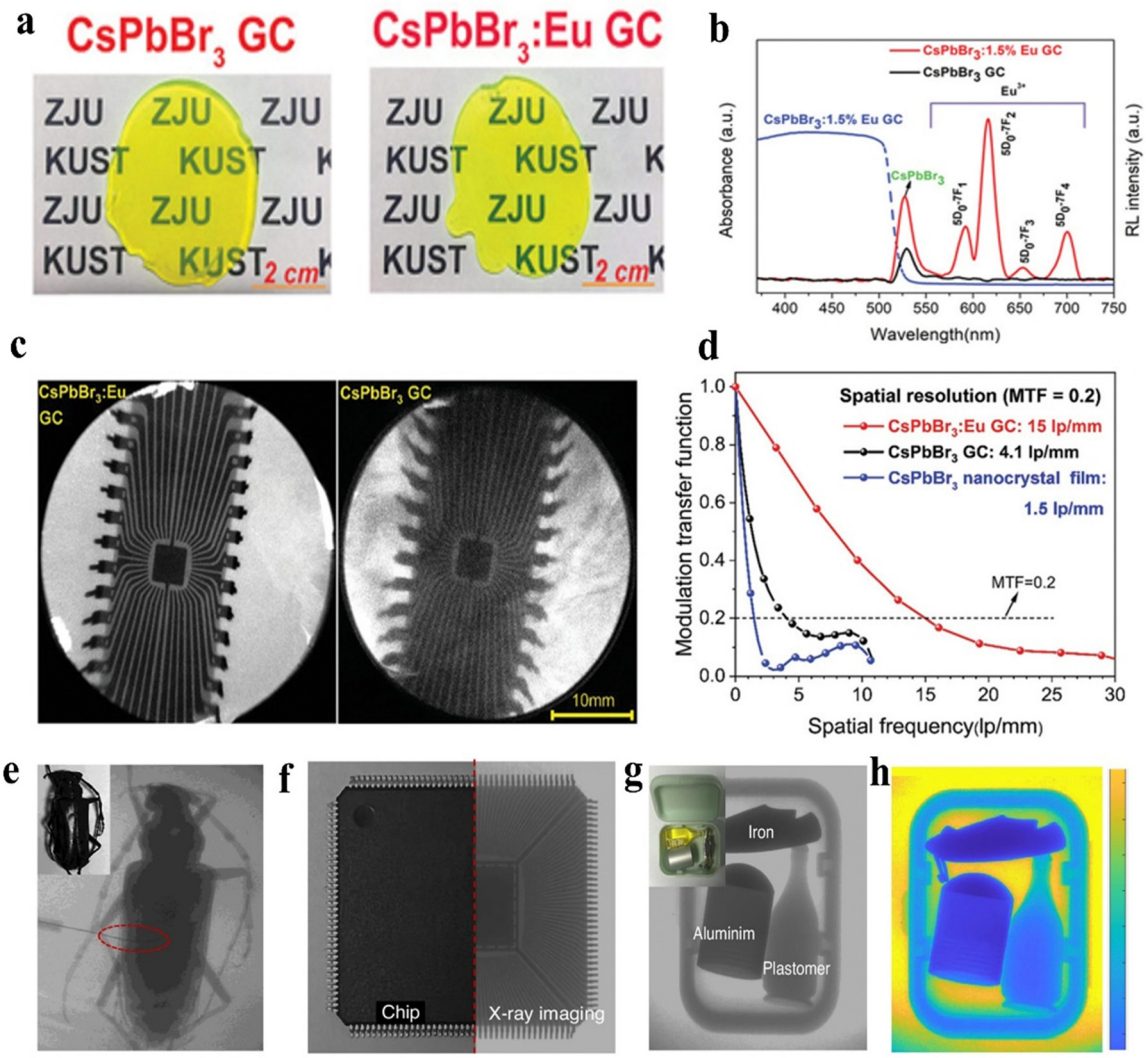

Fig. 5 (a) Photographs of $CsPbBr_3$-GC glass ceramics and $CsPbBr_3$:1.5%Eu-GC. (b) Radioluminescence spectra of $CsPbBr_3$-GC and $CsPbBr_3$:1.5%Eu-GC under X-ray irradiation. Corresponding absorption spectra are presented to demonstrate the self-absorption effect. (c) and (d) Comparative analysis of radiographic performance and spatial resolution between $CsPbBr_3$-GC and $CsPbBr_3$:1.5%Eu-GC under X-ray irradiation.[93] (e) Longicorn specimens. (f) Chip driver. (g) Concealed objects in plastic box: coffee bottle, iron knife, and aluminum pot. (h) Multicolor imaging achieved *via* MATLAB-based simulation.[94] (Adapted with permission from ref. 93. (Copyright 2021, Wiley-VCH GmbH) and ref. 94 (Copyright 2024, Springer Nature)).

5.2. X-ray detection

A scintillator detector is typically composed of scintillator crystals, photomultiplier tubes, and preamplifier circuits. Scintillator detectors are primarily categorized into direct and indirect types based on their detection mechanisms. All radiation detectors operate based on the fundamental principle of converting radiation into measurable electrical or optical signals, which can then be amplified and processed by standard electronic systems. Rare earth ion doping effectively reduces crystal defects in MHPs single crystals, enhances carrier mobility, and thereby improves the detection sensitivity of MHP-based optoelectronic devices. Zi *et al.* synthesized $MAPbI_3$:Yb^{3+}, $MAPbI_3$:Er^{3+}, and $MAPbI_3$:Yb^{3+}/Er^{3+} single crystals *via* the solvothermal method.[95] The $MAPbI_3$:Yb^{3+}/Er^{3+} devices demonstrated multi-mode detection capabilities across visible, near-infrared, and X-ray spectral regions. When used as an X-ray detector (Fig. 6a–c), the $MAPbI_3$:Yb^{3+}/Er^{3+} single crystal exhibited a photocurrent of 0.71 mA cm^{-2} under 1 V bias at an X-ray dose rate of 2.41 mGy s^{-1}, compared to 0.23 mA cm^{-2} for the undoped counterpart. The detection sensitivity reached 1.16×10^6 $\mu CGy^{-1}cm^{-2}$ under an applied electric field of −3 V mm^{-1}, representing a 2.7-fold improvement over undoped crystals.

Currently, the radiation detection performance of $MAPbI_3$ significantly lags behind that of $MAPbBr_3$, despite its promising material characteristics.[97] While halogen doping at the X-site has been extensively studied in three-dimensional MHPs, cation doping at the A-site remains comparatively rare. To address this, Yuan *et al.* successfully synthesized centimeter-scale DMAMAPbI$_3$ (DMA = dimethylammonium) and GAMAPbI$_3$ (GA = guanidinium) alloys through strategic incorporation of large-sized cations

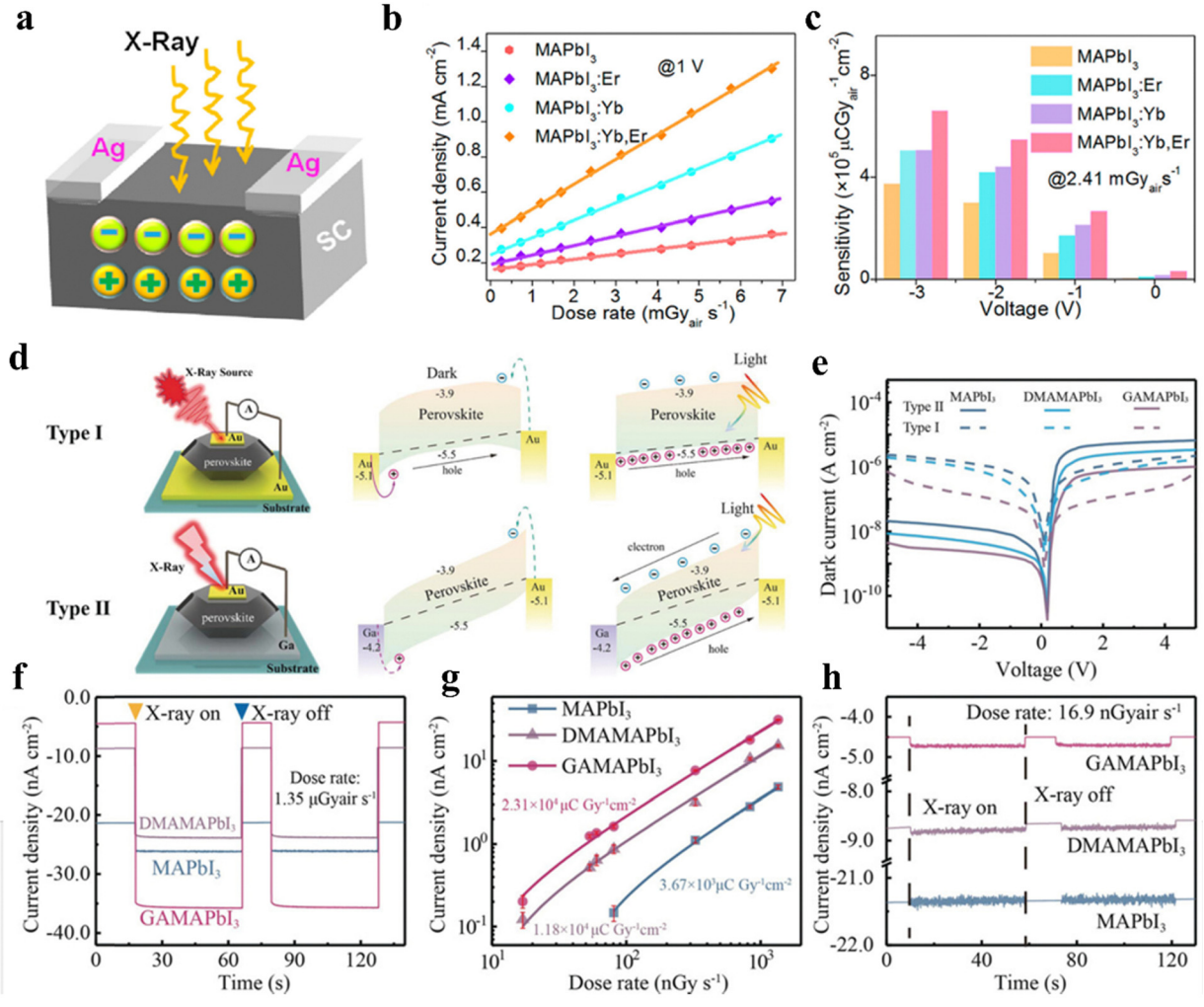

Fig. 6 (a) Structural diagrams of undoped $MAPbI_3$ and $MAPbI_3$:RE^{3+} planar electrode X-ray detectors. (b) Photocurrent intensity *versus* radiation dose rate characteristics for undoped $MAPbI_3$ and $MAPbI_3$:RE^{3+} devices under 1 V bias. (c) Sensitivity comparison between undoped $MAPbI_3$ and $MAPbI_3$:RE^{3+} X-ray detectors under 2.41 mGy s^{-1} dose rate with varying bias voltages.[95] (d) Device architectures of $MAPbI_3$-based detectors: type I (symmetric electrode) and type II (asymmetric electrode). (e) Dark current–voltage characteristics of symmetric and asymmetric device configurations. (f) X-ray response characteristics of the device under 1.35 μGy s^{-1} dose rate. (g) X-ray dose rate dependent photocurrent responses of pristine and doped devices. (h) Photoresponse switching characteristics of pristine and doped devices under 16.9 nGy s^{-1} dose rate.[96] (Adapted with permission from ref. 95. (Copyright 2022, American Chemical Society) and ref. 96 (Copyright 2019, Wiley-VCH Verlag GmbH & Co. KGaA, Weinheim)).

at the A-site.[96] The minimum detectable dose rate serves as the most critical performance indicator for X-ray detectors, exhibiting strong correlation with the dark current of the device. Consequently, judicious selection of detector architecture becomes essential for dark current minimization. Fig. 6d illustrates that the minimum conduction band and maximum valence band of $MAPbI_3$ are positioned at −3.9 eV and −5.5 eV, respectively. Based on these energy levels and doping characteristics, an asymmetric Ga/$MAPbI_3$/Au electrode configuration was engineered to suppress the leakage current (Fig. 6d). The asymmetric electrode architecture enabled $DMAMAPbI_3$ and $GAMAPbI_3$ devices to achieve reduced dark current densities, as demonstrated in Fig. 6e. Under 1.35 μGy s^{-1} irradiation, $DMAMAPbI_3$ and $GAMAPbI_3$ devices generated photocurrents of 15.2 nA and 31.3 nA, respectively, representing significant enhancement over conventional $MAPbI_3$ detectors (Fig. 6f). At the same time, $GAMAPbI_3$ not only showed the highest detector sensitivity (2.3 × 104 μCGy^{-1} cm^{-2}), but also exhibited an extremely low detection limit (16.9 nGy s^{-1}), as shown in Fig. 6g and h. In addition, the performance of current radiation detectors was enhanced by more than an order of magnitude.

5.3. α-/β-particle detection

In recent years, the design of MHPs-based particle detectors has achieved significant progress, including α-particle[98,99] and β-particle detectors.[100] Dang *et al.* pioneered the investigation of α-particle detection using Li-doped $(PEA)_2PbBr_4$ scintillators.[101] When irradiated with ^{241}Am (5486 keV) and ^{244}Cm (5805 keV) radiation sources, two distinct peaks can be clearly observed, as shown in Fig. 7a. Fig. 7b displays the pulse shape discrimination plot for the Li-doped $(PEA)_2PbBr_4$ crystal. The α-particle signals in the high-energy channel demonstrate

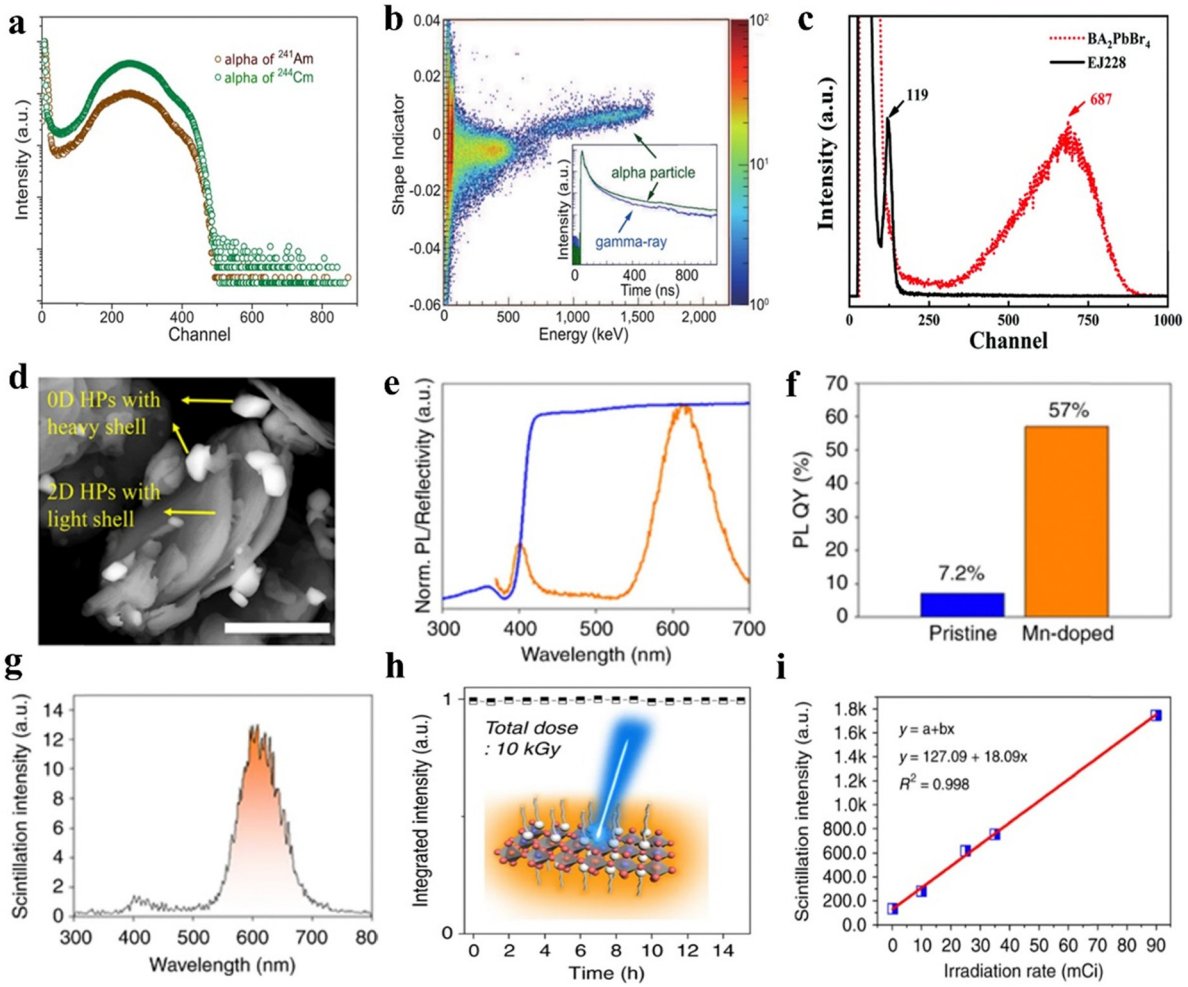

Fig. 7 (a) α particle pulse height spectrum of the $(BA)_2PbBr_4$ scintillator. (b) Pulse shape discrimination matrix showing the shape indicator (*Y*-axis) *versus* measured energy in electronic equivalent units.[101] (c) Pulse height spectra comparison between $(BA)_2PbBr_4$ microcrystals and EJ228 plastic scintillator under ^{237}Np excitation.[102] (d) Backscattered electron SEM images of perovskite NCs ($CsPbBr_3/Cs_4PbBr_6$) and 2D perovskite $(STA)_2PbBr_4$ (scale bar: 5 μm). (e) Normalized photoluminescence and reflectance spectra of the Mn(II)-doped 2D perovskite. (f) Enhancement of the PLQY following Mn(II) incorporation. (g) Flicker performance of STA_2PbBr_4. (h) High beta hardness. (i) Linear response of the scintillator under detection limits.[100] (Adapted with permission from ref. 101. (Copyright 2020, Springer Nature),[102] (Copyright 2021, Royal Society of Chemistry) and ref. 100 (Copyright 2020, Springer Nature)).

effective separation from gamma-ray signals. Furthermore, the BA_2PbBr_4 crystal exhibits a pronounced signal peak under ^{237}Np α-particle excitation, displaying six-fold higher intensity compared to the EJ228 plastic scintillator (Fig. 7c).[102] Additionally, this material demonstrated high energy resolutions of 24.29% and 22.68% for ^{237}Np-α sources, coupled with rapid decay times of 1.7 ns (99.9%) and 7.61 ns (0.1%).

β-particles are high-energy electrons or positrons emitted from radioactive nuclides.[103] They exhibit medium penetration capacity, higher than that of α particles but lower than that of X-rays, making their detection crucial for radioactive contamination monitoring. Yu *et al.* reported the first MHPs β-particle scintillator,[100] and subsequently tested reference scintillation based on $CsPbBr_3/Cs_4PbBr_6$ perovskite core/shell NCs. Scanning electron microscopy images reveal distinct electron backscattering differences between 2D and high-Z MHPs NCs (Fig. 7d), with the 2D MHPs demonstrating lower backscattering intensity (reduced brightness). Mn^{2+} ion doping (0.3%) was employed to enhance the Stokes shift, thereby improving the PLQY while minimizing reabsorption. Also, the PLQY increased from below 10% in undoped MHPs to over 50% in Mn-doped counterparts. The long-chain STA_2PbBr_4 demonstrated superior β-particle scintillation light yield (24 000 photons per MeV) (Fig. 7e–g). Furthermore, the 2D MHP scintillators exhibited excellent linear response and remarkable radiation hardness under β-particle irradiation (Fig. 7h and i).

5.4. Other applications

Cation-doped MHPs scintillators demonstrate applications not only in X-ray imaging/detection, and particle detectors, but also

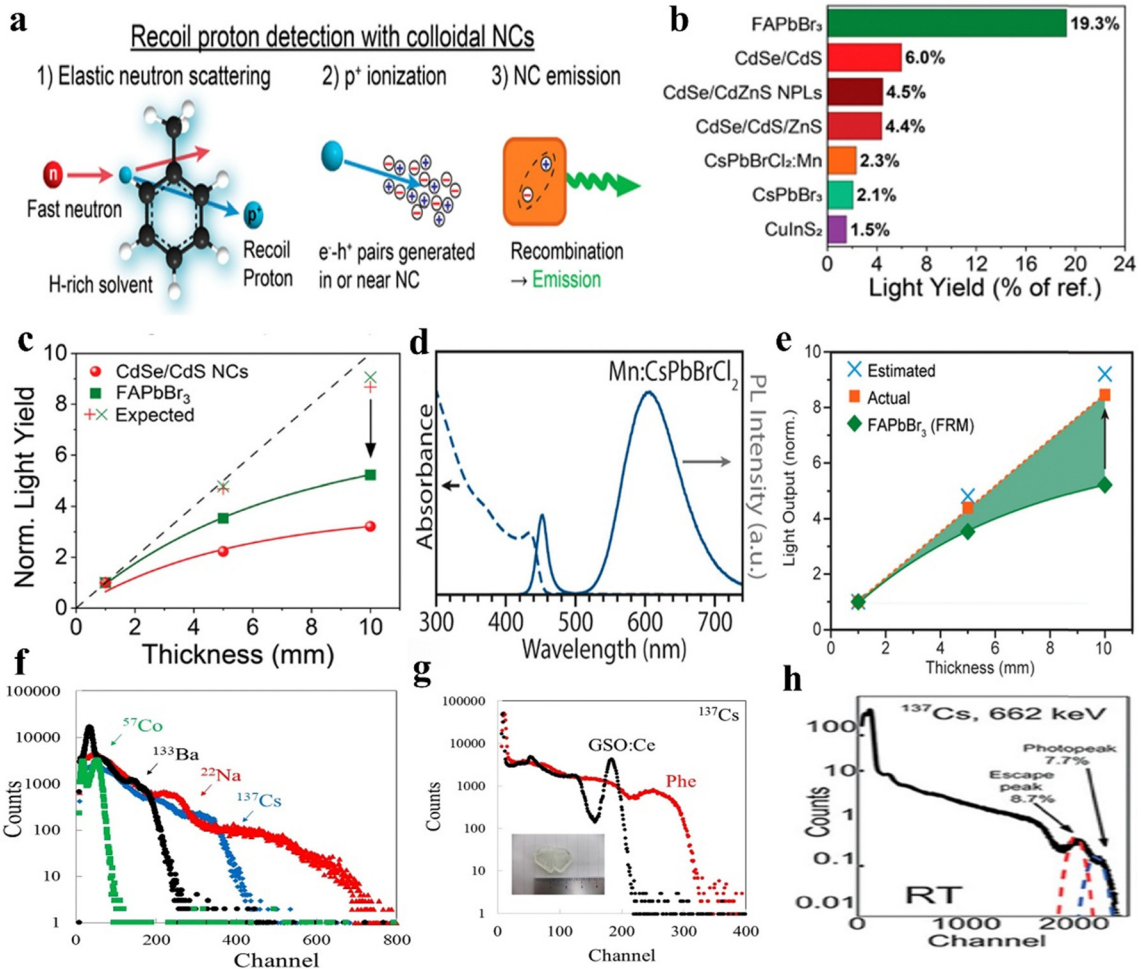

Fig. 8 (a) A schematic diagram illustrating the principle of fast neutron detection: (1) elastic scattering of fast neutrons on the H nuclei; (2) generation of charge carrier clouds through proton interactions; (3) NCs excitation and emission processes. (b) Comparative light yield of various NCs scintillators exposed to 300-second fast neutron beam irradiation. (c) Correlation between the normalized light yield ($FAPbBr_3$ *vs.* CdSe/CdS NCs) and scintillator thickness under full-concentration conditions.[104] (d) Optical characterization of Mn-doped $CsPbBrCl_2$ NCs: absorption and photoluminescence spectra. (e) Normalized light yield *versus* scintillator thickness demonstrates near-linear behavior for 66% Mn^{2+}:$CsPbBrCl_2$ NCs (orange squares), contrasting sharply with $FAPbBr_3$ NCs (green diamonds).[105] (f) Pulse height spectra of Phe at different gamma sources. (g) CS-induced Phe and GSO: pulse height spectra of Ce, illustrated by a photograph of a Phe crystal.[106] (h) Pulse height spectrum of Li-doped PEA_2PbBr_4 under 662 keV gamma radiation (^{137}Cs source).[107] (Adapted with permission from ref. 104. (Copyright 2020, American Chemical Society),[105] (Copyright 2021, American Chemical Society),[106] (Copyright 2017, Springer Nature),[107] (Copyright 2020, American Chemical Society)).

in neutron detection. For instance, McCall *et al.* pioneered the development of fast neutron scintillators using $FAPbBr_3$ and $CsPbBrCl_2$:Mn^{2+} NCs.[104] $FAPbBr_3$ exhibited the highest light yield (19% of the ZnS:Cu scintillator reference) attributed to their nearly uniform PLQY of 96% (Fig. 8a and b). While higher nanocrystal concentrations enhanced charge collection efficiency, the light output did not scale linearly with concentration due to significant reabsorption in $FAPbBr_3$ NCs (Fig. 8c). This strong reabsorption intensified light scattering, consequently reducing spatial resolution. In contrast, $CsPbBrCl_2$:Mn^{2+} NCs exhibited nearly twice the spatial resolution (27 *vs.* 52 pixels). Montanarella *et al.* subsequently optimized the synthesis process using long-chain zwitterionic ligands, achieving exceptional concentrations (>100 mg mL^{-1}) of $CsPbBrCl_2$:Mn NCs while preserving their Stokes shift advantages. The concentrated $CsPbBrCl_2$:Mn NCs maintained a PLQY of 53% with dominant Mn^{2+} emission (97% total emission) and a 1 eV Stokes shift (Fig. 8d). Furthermore, thickness and concentration-dependent measurements under fast neutron irradiation revealed the absence of self-absorption in this doped system, exhibiting an essentially linear concentration dependence and achieved drastically enhanced scalability, reaching $>91.9\%$ of the expected light yield at a 10-fold thickness increase (Fig. 8e). These results demonstrated that the Mn^{2+}-doped $CsPbBrCl_2$ NCs offer an unmatched combination of high concentration (>100 mg mL^{-1}), PLQY >50, and a large Stokes shift (~ 1 eV), enabling efficient fast-neutron scintillation.[105]

Cation-doped MHPs scintillators have demonstrated notable advancements in γ-ray detection. For instance, when compared to GSO:Ce scintillators, $(PEA)_2PbBr_4$ crystals exhibited superior performance with a luminous yield of 14 000 photons per MeV and a rapid decay time of 11 ns under 662 keV γ-ray irradiation.[106] As illustrated in Fig. 8f and g, $(PEA)_2PbBr_4$ crystals demonstrated significant responsiveness to multiple γ-ray sources, achieving an energy resolution of $35 \pm 5\%$ for 662 keV γ-rays. Furthermore, Li-doped $(PEA)_2PbBr_4$ crystals synthesized *via* the slow volatilization method revealed that Li^+ ion doping effectively enhanced their luminescence properties while suppressing their non-radiative transitions. The 1 : 1 Li-doped $(PEA)_2PbBr_4$ crystal demonstrated a remarkable light yield of 11 000 photons per MeV under 662 keV γ-ray exposure. This material displayed a rapid primary decay time of 11 ns and produced distinct light peaks with 12.4% energy resolution. Subsequent investigations by their team into Li-doped $(PEA)_2PbBr_4$ crystals achieved optimal performance showing the best energy resolution of 7.7% for 662 keV γ-ray (Fig. 8h).[107]

6. Challenges and prospects

Despite significant progress being made in cation doping engineering for MHPs scintillators, it is still in its infancy. Most A-site doping is limited to a few existing organic molecules, such as MA and FA. More suitable sized inorganic cations and organic groups can be explored to stabilize the phase structure of MHPs. Future research may draw inspiration from interfacial molecular engineering of rare earth-doped NCs, where tailored organic–inorganic hybrids achieve precise energy transfer and multifunctionality through advanced ligand design.[108] At present, B-site doping is an effective strategy to improve the scintillation performance of MHPs. However, in lead-based MHPs scintillators, the practical application is still not up to the standard, especially the stability and toxicity problems. In addition, although different cations have been doped into MHPs scintillators, the exact structural information associated with the doped ions, including but not limited to the exact crystal position occupied by the doped ions and their distribution in MHPs scintillators, has remained elusive in most cases. To obtain a reasonable understanding of doping-induced property changes, great efforts are needed to characterize the configuration of MHPs, especially in the local environment of doped cations. Such understanding will pave the way for targeted optimization of the scintillation properties of MHPs as well as theory-guided screening of dopant species. In addition, the influence and action mechanism of cation doping are still controversial and special, so it is necessary to explore the correct mechanism and guide the experiment correctly. Although cation doped MHPs scintillators are still far from practical application, they still can become the cornerstone of next-generation optoelectronic devices. Therefore, more efforts are needed to ensure that cation doped MHPs scintillators meet the requirements of the next generation commercial and industrial optoelectronic devices.

In summary, we have reviewed the recent research progress of cation doped MHPs scintillators, including A-site doping and B-site doping. The construction strategies of cation doped MHPs scintillators have also been discussed. Afterwards, we showed in detail the positive impact of cationic doping engineering on the scintillation properties of MHPs, which has greatly advanced their applications in the field of X-ray imaging/detection and particle detection. We hope that this review will inspire researchers to explore the next generation of cation doped MHPs scintillators and expand their applications.

Author contributions

Guiqiang Pu and Jiacheng Wang proposed the review topic and supervised the manuscript. Guiqiang Pu, Rufeng Wang, Junnan Song and Yangmin Tang wrote the manuscript. Guiqiang Pu and Junnan Song revised the manuscript. Guiqiang Pu and Jiacheng Wang modified and checked the format. All authors contributed to discussions and manuscript review.

Data availability

No primary research results, software or code have been included and no new data were generated or analysed as part of this review.

Conflicts of interest

There are no conflicts to declare.

Acknowledgements

The authors are grateful for the financial support from the National Natural Science Foundation of China (52472231 and 22402144) and the Central Guidance on Science and Technology Development Fund of Zhejiang Province (2024ZY01011).

Notes and references

1 M. Deng, Y. Tang, J. Chen, Y. Tang, J. Wang, T. Sun, M. Wang, J. Zhu, Z. Zhou and J. Wang, Bismuth Vacancy-Induced Enhancement of Luminescence Intensity and Irradiation Resistance for $Bi_4Ge_3O_{12}$, *J. Phys. Chem. Lett.*, 2023, **14**, 3818–3825.

2 N. Gan, X. Zou, M. Dong, Y. Wang, X. Wang, A. Lv, Z. Song, Y. Zhang, W. Gong, Z. Zhao, Z. Wang, Z. Zhou, H. Ma, X. Liu, Q. Chen, H. Shi, H. Yang, L. Gu, Z. An and W. Huang, Organic phosphorescent scintillation from copolymers by X-ray irradiation, *Nat. Commun.*, 2022, **13**, 3995.

3 B. D. Milbrath, A. J. Peurrung, M. Bliss and W. J. Weber, Radiation detector materials: An overview, *J. Mater. Res.*, 2008, **23**, 2561–2581.

4 R. Hofstadter, Alkali Halide Scintillation Counters, *Phys. Rev.*, 1948, **74**, 100–101.

5 M. Laval, M. Moszyński, R. Allemand, E. Cormoreche, P. Guinet, R. Odru and J. Vacher, Barium fluoride—Inorganic scintillator for subnanosecond timing, *Nucl. Instrum. Methods Phys. Res.*, 1983, **206**, 169–176.

6 W. Drozdowski, A. J. Wojtowicz, S. Ł. M. Kaczmarek and M. Berkowski, Scintillation yield of $Bi_4Ge_3O_{12}$ (BGO) pixel crystals, *Phys. B*, 2010, **405**, 1647–1651.

7 A. A. Naqvi, Z. Kalakada, M. S. Al-Anezi, M. Raashid, R. Khateeb ur, M. Maslehuddin and M. A. Garwan, Low energy prompt gamma-ray tests of a large volume BGO detector, *Appl. Radiat. Isot.*, 2012, **70**, 222–226.

8 A. R. Chakhmouradian and P. M. Woodward, Celebrating 175 years of perovskite research: a tribute to Roger H. Mitchell, *Phys. Chem. Miner.*, 2014, **41**, 387–391.

9 W. Li, Z. Wang, F. Deschler, S. Gao, R. H. Friend and A. K. Cheetham, Chemically diverse and multifunctional hybrid organic–inorganic perovskites, *Nat. Rev. Mater.*, 2017, **2**, 1–18.

10 V. Kumar and Z. Luo, A Review on X-ray Excited Emission Decay Dynamics in Inorganic Scintillator Materials, *Photonics*, 2021, **8**, 71.

11 Q. Chen, J. Wu, X. Ou, B. Huang, J. Almutlaq, A. A. Zhumekenov, X. Guan, S. Han, L. Liang, Z. Yi, J. Li, X. Xie, Y. Wang, Y. Li, D. Fan, D. B. L. Teh, A. H. All, O. F. Mohammed, O. M. Bakr, T. Wu, M. Bettinelli, H. Yang, W. Huang and X. Liu, All-inorganic perovskite nanocrystal scintillators, *Nature*, 2018, **561**, 88–93.

12 J. Ma, W. Zhu, L. Lei, D. Deng, Y. Hua, Y. M. Yang, S. Xu and P. N. Prasad, Highly Efficient $NaGdF_4$:Ce/Tb Nanoscintillator with Reduced Afterglow and Light Scattering for High-Resolution X-ray Imaging, *ACS Appl. Mater. Interfaces*, 2021, **13**, 44596–44603.

13 H. Huang, M. I. Bodnarchuk, S. V. Kershaw, M. V. Kovalenko and A. L. Rogach, Lead Halide Perovskite Nanocrystals in the Research Spotlight: Stability and Defect Tolerance, *ACS Energy Lett.*, 2017, **2**, 2071–2083.

14 J. Song, J. Li, J. Xu and H. Zeng, Superstable Transparent Conductive Cu@Cu_4Ni Nanowire Elastomer Composites against Oxidation, Bending, Stretching, and Twisting for Flexible and Stretchable Optoelectronics, *Nano Lett.*, 2014, **14**, 6298–6305.

15 J. Song, S. A. Kulinich, J. Li, Y. Liu and H. Zeng, A General One-Pot Strategy for the Synthesis of High-Performance Transparent-Conducting-Oxide Nanocrystal Inks for All-Solution-Processed Devices, *Angew. Chem., Int. Ed.*, 2015, **54**, 462–466.

16 D. J. Kubicki, D. Prochowicz, A. Hofstetter, S. M. Zakeeruddin, M. Grätzel and L. Emsley, Phase Segregation in Cs-, Rb- and K-Doped Mixed-Cation $(MA)_x(FA)_{1-x}PbI_3$ Hybrid Perovskites from Solid-State NMR, *J. Am. Chem. Soc.*, 2017, **139**, 14173–14180.

17 D. Amgar, T. Binyamin, V. Uvarov and L. Etgar, Near ultraviolet to mid-visible band gap tuning of mixed cation $Rb_xCs_{1-x}PbX_3$ (X = Cl or Br) perovskite nanoparticles, *Nanoscale*, 2018, **10**, 6060–6068.

18 D. Chen, X. Chen, Z. Wan and G. Fang, Full-Spectral Fine-Tuning Visible Emissions from Cation Hybrid Cs1–mFAmPbX3 (X = Cl, Br, and I, $0 \leq m \leq 1$) Quantum Dots, *ACS Appl. Mater. Interfaces*, 2017, **9**, 20671–20678.

19 C. Li, C. Chen, W. Gao, H. Dong, Y. Zhou, Z. Wu and C. Ran, Wide-Bandgap Lead Halide Perovskites for Next-Generation Optoelectronics: Current Status and Future Prospects, *ACS Nano*, 2024, **18**, 35130–35163.

20 X. Lu, R. Lin, Y. Ding, M. Xia, W. Zheng and F. Huang, Mixed low-dimensional metal halide perovskite single crystal for low-detection-limit x-ray detection *via* oriented ion migration, *InfoMat*, 2024, **6**, e12604.

21 X. Song, S. Liu, L. Ren, Y. Zuo, S. Wang, E. Wang, J. Qian, T. Ye, K. Wang and C. Wu, Two-dimensionalization of 3D perovskites for passive narrowband Photodetection, *EcoMat*, 2024, **6**, e12472.

22 J. Kang and L.-W. Wang, High Defect Tolerance in Lead Halide Perovskite $CsPbBr_3$, *J. Phys. Chem. Lett.*, 2017, **8**, 489–493.

23 Y. Zhou, J. Chen, O. M. Bakr and H.-T. Sun, Metal-Doped Lead Halide Perovskites: Synthesis, Properties, and Optoelectronic Applications, *Chem. Mater.*, 2018, **30**, 6589–6613.

24 R. Yun, H. Yang, W. Sun, L. Zhang, X. Liu, X. Zhang and X. Li, Recent Advances on Mn^{2+}-Doping in Diverse Metal Halide Perovskites, *Laser Photonics Rev.*, 2023, **17**, 2200524.

25 W.-J. Yin, B. Weng, J. Ge, Q. Sun, Z. Li and Y. Yan, Oxide perovskites, double perovskites and derivatives for electrocatalysis, photocatalysis, and photovoltaics, *Energy Environ. Sci.*, 2019, **12**, 442–462.

26 H. Dong, C. Ran, W. Gao, M. Li, Y. Xia and W. Huang, Metal Halide Perovskite for next-generation optoelectronics: progresses and prospects, *eLight*, 2023, **3**, 3.

27 C. Zhou, H. Lin, Q. He, L. Xu, M. Worku, M. Chaaban, S. Lee, X. Shi, M.-H. Du and B. Ma, Low dimensional metal

halide perovskites and hybrids, *Mater. Sci. Eng., R.*, 2019, **137**, 38–65.
28 W. Travis, E. N. K. Glover, H. Bronstein, D. O. Scanlon and R. G. Palgrave, On the application of the tolerance factor to inorganic and hybrid halide perovskites: a revised system, *Chem. Sci.*, 2016, **7**, 4548–4556.
29 Y. Wei, Z. Cheng and J. Lin, An overview on enhancing the stability of lead halide perovskite quantum dots and their applications in phosphor-converted LEDs, *Chem. Soc. Rev.*, 2019, **48**, 310–350.
30 M.-G. Ju, J. Dai, L. Ma and X. C. Zeng, Lead-Free Mixed Tin and Germanium Perovskites for Photovoltaic Application, *J. Am. Chem. Soc.*, 2017, **139**, 8038–8043.
31 A. Dutta, R. K. Behera, S. K. Dutta, S. Das Adhikari and N. Pradhan, Annealing $CsPbX_3$ (X = Cl and Br) Perovskite Nanocrystals at High Reaction Temperatures: Phase Change and Its Prevention, *J. Phys. Chem. Lett.*, 2018, **9**, 6599–6604.
32 Z. Shi, J. Guo, Y. Chen, Q. Li, Y. Pan, H. Zhang, Y. Xia and W. Huang, Lead-Free Organic–Inorganic Hybrid Perovskites for Photovoltaic Applications: Recent Advances and Perspectives, *Adv. Mater.*, 2017, **29**, 1605005.
33 C. Li, X. Lu, W. Ding, L. Feng, Y. Gao and Z. Guo, Formability of ABX_3 (X = F, Cl, Br, I) halide perovskites, *Acta Crystallogr., Sect. B: Struct. Sci.*, 2008, **64**, 702–707.
34 A. Hazarika, Q. Zhao, E. A. Gaulding, J. A. Christians, B. Dou, A. R. Marshall, T. Moot, J. J. Berry, J. C. Johnson and J. M. Luther, Perovskite Quantum Dot Photovoltaic Materials beyond the Reach of Thin Films: Full-Range Tuning of A-Site Cation Composition, *ACS Nano*, 2018, **12**, 10327–10337.
35 G. Volonakis, M. R. Filip, A. A. Haghighirad, N. Sakai, B. Wenger, H. J. Snaith and F. Giustino, Lead-Free Halide Double Perovskites *via* Heterovalent Substitution of Noble Metals, *J. Phys. Chem. Lett.*, 2016, **7**, 1254–1259.
36 A. Swarnkar, W. J. Mir and A. Nag, Can B-Site Doping or Alloying Improve Thermal- and Phase-Stability of All-Inorganic CsPbX3 (X = Cl, Br, I) Perovskites?, *ACS Energy Lett.*, 2018, **3**, 286–289.
37 X. Zheng, C. Wu, S. K. Jha, Z. Li, K. Zhu and S. Priya, Improved Phase Stability of Formamidinium Lead Triiodide Perovskite by Strain Relaxation, *ACS Energy Lett.*, 2016, **1**, 1014–1020.
38 N. K. Kumawat, A. Dey, A. Kumar, S. P. Gopinathan, K. L. Narasimhan and D. Kabra, Band Gap Tuning of $CH_3NH_3Pb(Br_{1-x}Cl_x)_3$ Hybrid Perovskite for Blue Electroluminescence, *ACS Appl. Mater. Interfaces*, 2015, **7**, 13119–13124.
39 K. Hills-Kimball, Y. Nagaoka, C. Cao, E. Chaykovsky and O. Chen, Synthesis of formamidinium lead halide perovskite nanocrystals through solid–liquid–solid cation exchange, *J. Mater. Chem. C*, 2017, **5**, 5680–5684.
40 H. Huang, Y. Yang, S. Qiao, X. Wu, Z. Chen, Y. Chao, K. Yang, W. Guo, Z. Luo, X. Song, Q. Chen, C. Yang, Y. Yu and Z. Zou, Accommodative Organoammonium Cations in A-Sites of Sb–In Halide Perovskite Derivatives for Tailoring BroadBand Photoluminescence with X-Ray Scintillation and White-Light Emission, *Adv. Funct. Mater.*, 2024, **34**, 2309112.
41 Y. Huang, L. Qiao, Y. Jiang, T. He, R. Long, F. Yang, L. Wang, X. Lei, M. Yuan and J. Chen, A-site Cation Engineering for Highly Efficient $MAPbI_3$ Single-Crystal X-ray Detector, *Angew. Chem., Int. Ed.*, 2019, **58**, 17834–17842.
42 Y. Gao, Q. Cai, Y. He, D. Zhang, Q. Cao, M. Zhu, Z. Ma, B. Zhao, H. He, D. Di, Z. Ye and X. Dai, Highly efficient blue light-emitting diodes based on mixed-halide perovskites with reduced chlorine defects, *Sci. Adv.*, 2024, **10**, eado5645.
43 C. Otero-Martínez, M. Imran, N. J. Schrenker, J. Ye, K. Ji, A. Rao, S. D. Stranks, R. L. Z. Hoye, S. Bals, L. Manna, J. Pérez-Juste and L. Polavarapu, Fast A-Site Cation Cross-Exchange at Room Temperature: Single-to Double- and Triple-Cation Halide Perovskite Nanocrystals, *Angew. Chem., Int. Ed.*, 2022, **61**, e202205617.
44 Y. Ogomi, A. Morita, S. Tsukamoto, T. Saitho, N. Fujikawa, Q. Shen, T. Toyoda, K. Yoshino, S. S. Pandey, T. Ma and S. Hayase, $CH_3NH_3Sn_xPb_{(1-x)}I_3$ Perovskite Solar Cells Covering up to 1060 nm, *J. Phys. Chem. Lett.*, 2014, **5**, 1004–1011.
45 F. Hao, C. C. Stoumpos, R. P. H. Chang and M. G. Kanatzidis, Anomalous Band Gap Behavior in Mixed Sn and Pb Perovskites Enables Broadening of Absorption Spectrum in Solar Cells, *J. Am. Chem. Soc.*, 2014, **136**, 8094–8099.
46 C. Liu, J. Fan, H. Li, C. Zhang and Y. Mai, Highly Efficient Perovskite Solar Cells with Substantial Reduction of Lead Content, *Sci. Rep.*, 2016, **6**, 35705.
47 A. B. F. Vitoreti, S. Agouram, M. Solis de la Fuente, V. Muñoz-Sanjosé, M. A. Schiavon and I. Mora-Seró, Study of the Partial Substitution of Pb by Sn in Cs–Pb–Sn–Br Nanocrystals Owing to Obtaining Stable Nanoparticles with Excellent Optical Properties, *J. Phys. Chem. C*, 2018, **122**, 14222–14231.
48 H. Xu, W. Liang, Z. Zhang, C. Cao, W. Yang, H. Zeng, Z. Lin, D. Zhao and G. Zou, 2D Perovskite Mn^{2+}-Doped $Cs_2CdBr_2Cl_2$ Scintillator for Low-Dose High-Resolution X-ray Imaging, *Adv. Mater.*, 2023, **35**, 2300136.
49 J. Zhang, Q. Di, J. Liu, B. Bai, J. Liu, M. Xu and J. Liu, Heterovalent Doping in Colloidal Semiconductor Nanocrystals: Cation-Exchange-Enabled New Accesses to Tuning Dopant Luminescence and Electronic Impurities, *J. Phys. Chem. Lett.*, 2017, **8**, 4943–4953.
50 W. Zhu, W. Ma, Y. Su, Z. Chen, X. Chen, Y. Ma, L. Bai, W. Xiao, T. Liu, H. Zhu, X. Liu, H. Liu, X. Liu and Y. (Michael) Yang, Low-dose real-time X-ray imaging with nontoxic double perovskite scintillators, *Light Sci. Appl.*, 2020, **9**, 1–10.
51 G. Pan, X. Bai, D. Yang, X. Chen, P. Jing, S. Qu, L. Zhang, D. Zhou, J. Zhu, W. Xu, B. Dong and H. Song, Doping Lanthanide into Perovskite Nanocrystals: Highly Improved and Expanded Optical Properties, *Nano Lett.*, 2017, **17**, 8005–8011.

52 H. Arfin, J. Kaur, T. Sheikh, S. Chakraborty and A. Nag, Bi^{3+}-Er^{3+} and Bi^{3+}-Yb^{3+} Codoped $Cs_2AgInCl_6$ Double Perovskite Near-Infrared Emitters, *Angew. Chem., Int. Ed.*, 2020, **59**, 11307–11311.

53 M. Liu, N. Jiang, H. Huang, J. Lin, F. Huang, Y. Zheng and D. Chen, Ni^{2+}-doped $CsPbI_3$ perovskite nanocrystals with near-unity photoluminescence quantum yield and superior structure stability for red light-emitting devices, *Chem. Eng. J.*, 2021, **413**, 127547.

54 X. Wu, J. Sun, H. Shao, Y. Zhai, L. Li, W. Chen, J. Zhu, B. Dong, L. Xu, D. Zhou, W. Xu, H. Song and X. Bai, Self-powered UV photodetectors based on $CsPbCl_3$ nanowires enabled by the synergistic effect of acetate and lanthanide ion passivation, *Chem. Eng. J.*, 2021, **426**, 131310.

55 S. Yuan, T. Fang, J. Huang, X. Li, C. Wei, Y. Zhou, Y. Li, X. Zheng, J. Huang, J. Su, G. Baryshnikov, W. C. H. Choy, H. Zeng and B. Xu, Balancing Charge Injection *via* a Tailor-Made Electron-Transporting Material for High Performance Blue Perovskite QLEDs, *ACS Energy Lett.*, 2023, **8**, 818–826.

56 D. S. Dolzhnikov, C. Wang, Y. Xu, M. G. Kanatzidis and E. A. Weiss, Ligand-Free, Quantum-Confined Cs_2SnI_6 Perovskite Nanocrystals, *Chem. Mater.*, 2017, **29**, 7901–7907.

57 R. Begum, X. Y. Chin, M. Li, B. Damodaran, T. C. Sum, S. Mhaisalkar and N. Mathews, Stable Sn2+ doped FAPbI3 nanocrystals for near-infrared LEDs, *Chem. Commun.*, 2019, **55**, 5451–5454.

58 X. Tang, Z. Hu, W. Chen, X. Xing, Z. Zang, W. Hu, J. Qiu, J. Du, Y. Leng, X. Jiang and L. Mai, Room temperature single-photon emission and lasing for all-inorganic colloidal perovskite quantum dots, *Nano Energy*, 2016, **28**, 462–468.

59 T. J. Milstein, D. M. Kroupa and D. R. Gamelin, Picosecond Quantum Cutting Generates Photoluminescence Quantum Yields Over 100% in Ytterbium-Doped $CsPbCl_3$ Nanocrystals, *Nano Lett.*, 2018, **18**, 3792–3799.

60 Y. Zhao, T. Tian, Z. Zhang, S. Li and L. Wang, Boosting the Synthetic Yield and Stability of $CsPbBr_3$ Nanocrystals *via* Solvent Injection Quenching for Future Microscale Displays, *ACS Appl. Nano Mater.*, 2022, **5**, 11889–11895.

61 G. Huang, C. Wang, S. Xu, S. Zong, J. Lu, Z. Wang, C. Lu and Y. Cui, Postsynthetic Doping of $MnCl_2$ Molecules into Preformed $CsPbBr_3$ Perovskite Nanocrystals *via* a Halide Exchange-Driven Cation Exchange, *Adv. Mater.*, 2017, **29**, 1700095.

62 F. Li, Z. Xia, Y. Gong, L. Gu and Q. Liu, Optical properties of Mn^{2+} doped cesium lead halide perovskite nanocrystals *via* a cation–anion co-substitution exchange reaction, *J. Mater. Chem. C*, 2017, **5**, 9281–9287.

63 F. Zhang, H. Zhong, C. Chen, X. Wu, X. Hu, H. Huang, J. Han, B. Zou and Y. Dong, Brightly Luminescent and Color-Tunable Colloidal $CH_3NH_3PbX_3$ (X = Br, I, Cl) Quantum Dots: Potential Alternatives for Display Technology, *ACS Nano*, 2015, **9**, 4533–4542.

64 X. Li, Y. Guo and B. Luo, Improved Stability and Photoluminescence Yield of Mn2+-Doped CH3NH3PbCl3 Perovskite Nanocrystals, *Crystals*, 2018, **8**, 1–10.

65 C. Zhou, Y. Tian, O. Khabou, M. Worku, Y. Zhou, J. Hurley, H. Lin and B. Ma, Manganese-Doped One-Dimensional Organic Lead Bromide Perovskites with Bright White Emissions, *ACS Appl. Mater. Interfaces*, 2017, **9**, 40446–40451.

66 W. J. Mir, M. Jagadeeswararao, S. Das and A. Nag, Colloidal Mn-Doped Cesium Lead Halide Perovskite Nanoplatelets, *ACS Energy Lett.*, 2017, **2**, 537–543.

67 G. E. Eperon and D. S. Ginger, B-Site Metal Cation Exchange in Halide Perovskites, *ACS Energy Lett.*, 2017, **2**, 1190–1196.

68 Q. Hu, Z. Li, Z. Tan, H. Song, C. Ge, G. Niu, J. Han and J. Tang, Rare Earth Ion-Doped $CsPbBr_3$ Nanocrystals, *Adv. Opt. Mater.*, 2018, **6**, 1700864.

69 Y. Cheng, C. Shen, L. Shen, W. Xiang and X. Liang, Tb^{3+}, Eu^{3+} Co-doped $CsPbBr_3$ QDs Glass with Highly Stable and Luminous Adjustable for White LEDs, *ACS Appl. Mater. Interfaces*, 2018, **10**, 21434–21444.

70 S.-H. Chan, M.-C. Wu, K.-M. Lee, W.-C. Chen, T.-H. Lin and W.-F. Su, Enhancing perovskite solar cell performance and stability by doping barium in methylammonium lead halide, *J. Mater. Chem. A*, 2017, **5**, 18044–18052.

71 C. F. J. Lau, M. Zhang, X. Deng, J. Zheng, J. Bing, Q. Ma, J. Kim, L. Hu, M. A. Green, S. Huang and A. Ho-Baillie, Strontium-Doped Low-Temperature-Processed $CsPbI_2Br$ Perovskite Solar Cells, *ACS Energy Lett.*, 2017, **2**, 2319–2325.

72 Z. Du, D. Fu, T. Yang, Z. Fang, W. Liu, F. Gao, L. Wang, Z. Yang, J. Teng, H. Zhang and W. Yang, Photodetectors with ultra-high detectivity based on stabilized all-inorganic perovskite $CsPb_{0.92}2Sn_{0.078I3}$ nanobelts, *J. Mater. Chem. C*, 2018, **6**, 6287–6296.

73 W. Shao, X. Wang, Z. Zhang, J. Huang, Z. Han, S. Pi, Q. Xu, X. Zhang, X. Xia and H. Liang, Highly Efficient and Flexible Scintillation Screen Based on Manganese (II) Activated 2D Perovskite for Planar and Nonplanar High-Resolution X-Ray Imaging, *Adv. Opt. Mater.*, 2022, **10**, 2102282.

74 W. Ma, T. Jiang, Z. Yang, H. Zhang, Y. Su, Z. Chen, X. Chen, Y. Ma, W. Zhu, X. Yu, H. Zhu, J. Qiu, X. Liu, X. Xu and Y. (Michael) Yang, Highly Resolved and Robust Dynamic X-Ray Imaging Using Perovskite Glass-Ceramic Scintillator with Reduced Light Scattering, *Adv. Sci.*, 2021, **8**, 2003728.

75 N. Li, Z. Xu, Y. Xiao, Y. Liu, Z. Yang and S. (Frank) Liu, Flexible, High Scintillation Yield $Cu_3Cu_2I_5$ Film Made of Ball-Milled Powder for High Spatial Resolution X-Ray Imaging, *Adv. Opt. Mater.*, 2022, **10**, 2102232.

76 B. Yang, L. Yin, G. Niu, J.-H. Yuan, K.-H. Xue, Z. Tan, X.-S. Miao, M. Niu, X. Du, H. Song, E. Lifshitz and J. Tang, Lead-Free Halide Rb_2CuBr_3 as Sensitive X-Ray Scintillator, *Adv. Mater.*, 2019, **31**, 1904711.

77 F. Zhang, Y. Zhou, Z. Chen, M. Wang, Z. Ma, X. Chen, M. Jia, D. Wu, J. Xiao, X. Li, Y. Zhang, Z. Shi and C. Shan, Thermally Activated Delayed Fluorescence Zirconium-Based Perovskites for Large-Area and Ultraflexible X-ray Scintillator Screens, *Adv. Mater.*, 2022, **34**, 2204801.

78 T. He, Y. Zhou, X. Wang, J. Yin, L. Gutiérrez-Arzaluz, J.-X. Wang, Y. Zhang, O. M. Bakr and O. F. Mohammed,

High-Performance Copper-Doped Perovskite-Related Silver Halide X-ray Imaging Scintillator, *ACS Energy Lett.*, 2022, **7**, 2753–2760.

79 Y. Chen, H. Yang, J. Song and B. Zhang, An effective Fe(II) doping strategy for stable and highly photoluminescent $CsPbBrI_2$ nanocrystals, *J. Mater. Chem. C*, 2022, **10**, 5147–5154.

80 H. Huang, Y. Yang, S. Qiao, X. Wu, Z. Chen, Y. Chao, K. Yang, W. Guo, Z. Luo, X. Song, Q. Chen, C. Yang, Y. Yu and Z. Zou, Accommodative Organoammonium Cations in A-Sites of Sb–In Halide Perovskite Derivatives for Tailoring BroadBand Photoluminescence with X-Ray Scintillation and White-Light Emission, *Adv. Funct. Mater.*, 2024, **34**, 2309112.

81 V. Naresh, P.-R. Cha and N. Lee, $Cs_2NaGdCl_6$:Tb^{3+}–A Highly Luminescent Rare-Earth Double Perovskite Scintillator for Low-Dose X-ray Detection and Imaging, *ACS Appl. Mater. Interfaces*, 2024, **16**, 19068–19080.

82 F. Maddalena, M. H. Mahyuddin, D. Kowal, M. E. Witkowski, M. Makowski, M. A. Kuddus Sheikh, S. Mahato, R. Jedrzejewski, W. Drozdowski, C. Dujardin, C. Dang and M. D. Birowosuto, Lattice Expansion in Rb-Doped Hybrid Organic–Inorganic Perovskite Crystals Resulting in Smaller Band-Gap and Higher Light-Yield Scintillators, *Inorg. Chem.*, 2023, **62**, 8892–8902.

83 W. Gui, L. Yao, X. Zhou and C. L. Wang, Defect modulation of stable and fast inorganic perovskite Rb_2AgCl_3 scintillators *via* Li^+ doping for X-ray imaging, *J. Alloys Compd.*, 2025, **1014**, 178667.

84 J. Zhang, L. Zhang, P. Cai, X. Xue, M. Wang, J. Zhang and G. Tu, Enhancing stability of red perovskite nanocrystals through copper substitution for efficient light-emitting diodes, *Nano Energy*, 2019, **62**, 434–441.

85 Y. Tong, M. Jin, Y. Chen, Y. Zhao, H. Yang, Q. Wang, L. Zhai, X. Liang and W. Xiang, Ultrastable and high colour rendering index WLEDs based on $CsPbBrI_2$ nanocrystals prepared by a two-step facile encapsulation method, *J. Mater. Chem. C*, 2021, **9**, 2530–2538.

86 J. Lu, S.-C. Chen and Q. Zheng, Defect passivation of $CsPbI_2Br$ perovskites through Zn(II) doping: toward efficient and stable solar cells, *Sci. China: Chem.*, 2019, **62**, 1044–1050.

87 C.-H. Lu, G. V. Biesold-McGee, Y. Liu, Z. Kang and Z. Lin, Doping and ion substitution in colloidal metal halide perovskite nanocrystals, *Chem. Soc. Rev.*, 2020, **49**, 4953–5007.

88 S. Tao, I. Schmidt, G. Brocks, J. Jiang, I. Tranca, K. Meerholz and S. Olthof, Absolute energy level positions in tin- and lead-based halide perovskites, *Nat. Commun.*, 2019, **10**, 1–10.

89 K. L. Svane, A. C. Forse, C. P. Grey, G. Kieslich, A. K. Cheetham, A. Walsh and K. T. Butler, How Strong Is the Hydrogen Bond in Hybrid Perovskites?, *J. Phys. Chem. Lett.*, 2017, **8**, 6154–6159.

90 Z. Chen, D. Lu, H. Xie, X. Yang, Y. Li, C. Bao, L. Lei and S. Xu, Triplet Exciton Enhanced Radioluminescence of Ga^{3+}/Tb^{3+} Metallacrown Scintillators for X-Ray Detection, *Adv. Opt. Mater.*, 2022, **10**, 2102074.

91 D. Wu, Y. Luo, P. He, K. An, J. Lai, P. Feng, M. Zhou, Y. Liu, X. Tang and G. Han, Ultrastable Lead-Free Rb_2AgCl_3 Microcrystals for X-ray Imaging, *ACS Appl. Opt. Mater.*, 2023, **1**, 78–84.

92 R. T. Williams, W. W. Wolszczak, X. Yan and D. L. Carroll, Perovskite Quantum-Dot-in-Host for Detection of Ionizing Radiation, *ACS Nano*, 2020, **14**, 5161–5169.

93 W. Ma, T. Jiang, Z. Yang, H. Zhang, Y. Su, Z. Chen, X. Chen, Y. Ma, W. Zhu, X. Yu, H. Zhu, J. Qiu, X. Liu, X. Xu and Y. (Michael) Yang, Highly Resolved and Robust Dynamic X-Ray Imaging Using Perovskite Glass-Ceramic Scintillator with Reduced Light Scattering, *Adv. Sci.*, 2021, **8**, 2003728.

94 K. Han, J. Jin, Y. Wang, X. Zhou, Y. Sun, L. Chen and Z. Xia, Hybrid Eu(II)-bromide scintillators with efficient 5d-4f band-gap transition for X-ray imaging, *Light: Sci. Appl.*, 2024, **13**, 222.

95 L. Zi, W. Xu, R. Sun, Z. Li, J. Zhang, L. Liu, N. Wang, Y. Wang, N. Ding, J. Hu, S. Lu, H. Zhu and H. Song, Lanthanide-Doped $MAPbI_3$ Single Crystals: Fabrication, Optical and Electrical Properties, and Multi-mode Photodetection, *Chem. Mater.*, 2022, **34**, 7412–7423.

96 Y. Huang, L. Qiao, Y. Jiang, T. He, R. Long, F. Yang, L. Wang, X. Lei, M. Yuan and J. Chen, A-site Cation Engineering for Highly Efficient MAPbI3 Single-Crystal X-ray Detector, *Angew. Chem., Int. Ed.*, 2019, **58**, 17834–17842.

97 F. Ye, H. Lin, H. Wu, L. Zhu, Z. Huang, D. Ouyang, G. Niu and W. C. H. Choy, High-Quality Cuboid $CH_3NH_3PbI_3$ Single Crystals for High Performance X-Ray and Photon Detectors, *Adv. Funct. Mater.*, 2019, **29**, 1806984.

98 K. M. McCall, Z. Liu, G. Trimarchi, C. C. Stoumpos, W. Lin, Y. He, I. Hadar, M. G. Kanatzidis and B. W. Wessels, α-Particle Detection and Charge Transport Characteristics in the A3M2I9 Defect Perovskites (A = Cs, Rb; M = Bi, Sb), *ACS Photonics*, 2018, **5**, 3748–3762.

99 B. Xiao, Q. Sun, S. Wang, L. Ji, Y. Li, S. Xi, B.-B. Zhang, J. Wang, W. Jie and Y. Xu, Two-Dimensional Dion–Jacobson Perovskite $(NH_3C_4H_8NH_3)CsPb_2Br_7$ with High X-ray Sensitivity and Peak Discrimination of α-Particles, *J. Phys. Chem. Lett.*, 2022, **13**, 1187–1193.

100 D. Yu, P. Wang, F. Cao, Y. Gu, J. Liu, Z. Han, B. Huang, Y. Zou, X. Xu and H. Zeng, Two-dimensional halide perovskite as β-ray scintillator for nuclear radiation monitoring, *Nat. Commun.*, 2020, **11**, 3395.

101 A. Xie, C. Hettiarachchi, F. Maddalena, M. E. Witkowski, M. Makowski, W. Drozdowski, A. Arramel, A. T. S. Wee, S. V. Springham, P. Q. Vuong, H. J. Kim, C. Dujardin, P. Coquet, M. D. Birowosuto and C. Dang, Lithium-doped two-dimensional perovskite scintillator for wide-range radiation detection, *Commun. Mater.*, 2020, **1**, 37.

102 Y. Li, L. Chen, B. Liu, P. Jin, R. Gao, L. Zhou, P. Wan, Q. Xu and X. Ouyang, Scintillation performance of two-dimensional perovskite $(BA)_2PbBr_4$ microcrystals, *J. Mater. Chem. C*, 2021, **9**, 17124–17128.

103 F. O. Ogundare and O. I. Adekoya, Gross alpha and beta radioactivity in surface soil and drinkable water around a

steel processing facility, *J. Radiat. Res. Appl. Sci.*, 2015, **8**, 411–417.

104 K. M. McCall, K. Sakhatskyi, E. Lehmann, B. Walfort, A. S. Losko, F. Montanarella, M. I. Bodnarchuk, F. Krieg, Y. Kelestemur, D. Mannes, Y. Shynkarenko, S. Yakunin and M. V. Kovalenko, Fast Neutron Imaging with Semiconductor Nanocrystal Scintillators, *ACS Nano*, 2020, **14**, 14686–14697.

105 F. Montanarella, K. M. McCall, K. Sakhatskyi, S. Yakunin, P. Trtik, C. Bernasconi, I. Cherniukh, D. Mannes, M. I. Bodnarchuk, M. Strobl, B. Walfort and M. V. Kovalenko, Highly Concentrated, Zwitterionic Ligand-Capped Mn^{2+}: $CsPb(Br_xCl_{1-x})_3$ Nanocrystals as Bright Scintillators for Fast Neutron Imaging, *ACS Energy Lett.*, 2021, **6**, 4365–4373.

106 N. Kawano, M. Koshimizu, G. Okada, Y. Fujimoto, N. Kawaguchi, T. Yanagida and K. Asai, Scintillating Organic–Inorganic Layered Perovskite-type Compounds and the Gamma-ray Detection Capabilities, *Sci. Rep.*, 2017, **7**, 14754.

107 A. Xie, F. Maddalena, M. E. Witkowski, M. Makowski, B. Mahler, W. Drozdowski, S. V. Springham, P. Coquet, C. Dujardin, M. D. Birowosuto and C. Dang, Library of Two-Dimensional Hybrid Lead Halide Perovskite Scintillator Crystals, *Chem. Mater.*, 2020, **32**, 8530–8539.

108 G. Pu, J. Song, Z. Cheng, Y. Tang, C. Kang and J. Wang, Interfacial Molecular Engineering of Rare Earth-doped Nanocrystals: Basic Principles, Construction Strategies, and Advanced Applications, *Laser Photonics Rev.*, 2025, 2500156.

